A High Wind Associated with Bow Echo Mesovortex over Cimenyan, Indonesia

Erma Yulihastin (erma.yulihastin@brin.go.id)
National Research and Innovation Agency https://orcid.org/0000-0001-5327-7597

Research Article

Keywords: small tornado, high wind, bow echo, mesovortex, Indonesia

Posted Date: October 10th, 2023

DOI: https://doi.org/10.21203/rs.3.rs-3424786/v1

Abstract

The high wind was noticed as the second natural disaster that frequently occurred during the last decade in the Indonesia Maritime Continent (IMC). However, the plausible mechanism of high wind still needed to be discovered due to the lack of observation measurements to detect the extreme event over a short time in a limited area over IMC. Herein, we investigated a high wind categorized as Beaufort 8 (56 km h^{-1}) with a devastating impact on 28 March 2021 in the meso-γ-scale over Cimenyan, Bandung, West Java, Indonesia. As the first documentation of a storm-induced high wind in IMC, we combined methods of observational and numerical using X-band radar and a high-resolution (0.2 km) of Weather Research and Forecasting (WRF) in studying the physical and dynamic processes related to that extreme event. Our finding pointed out that the high wind generated by an isolated system of a short-lived (40-minute) bow echo meso-γ-vortex is a precondition of mesoscale convective complex development on a synoptic scale. The bowing stage was initiated by a meso-convergence and genesis of meso-γ-vortex as mesoscale convergence vortices under the end-line theory developed by a sustained wind, vertical vorticity anomaly, strong vertical wind shear, and rotational updraft from low-to-surface levels of the troposphere. This study suggested that the WRF model with appropriate microphysics scheme and topography succeeded in simulating a real event of a short-lived bow-echo meso-γ-vortex with 10 minutes of early initial discrepancies between simulated and observed predicts better a storm-induced high wind for hydro-meteorological mitigation over IMC.

1. Introduction

In the recent decade, occurrences of the small tornado, so-called “puting beliung” in the Indonesian local wisdom term, increased in frequency and became the second hydro-meteorological disaster in Indonesia (BNPB, 2022). The whirlwind was occasionally reported as a high wind severely impacting residential construction. However, the plausible mechanism of the high wind was a lack of documentation due to a high resolution needed in time and space to explore the weather-related small-scale processes inconsiderate of season and location (Abdillah et al., 2022).

Even high winds have been documented in several regions randomly in Indonesia, the physical processes simplified as associated with a strong updraft related to an individual cumulonimbus intensification (Cahyanti et al., 2017; Lumbangaol et al., Prakosa & Nurjani, 2021). For Bandung, West Java, Indonesia, it is notable that high wind more frequently occurred over a certain area (i.e., Cimenyan) as recorded by the Regional Agency for Disaster Management (BPBD) of West Java Province about 5–7 times in a year (BPBD West Java, 2022). Since Cimenyan is located over a rugged topography in the north of Bandung basin and relatively close to the highland of Lembang District and mountains areas, the storm-induced high wind might have been developed by an enhancement of Mountain-Valley Breezes local circulation, which was mentioned in a previous study as a major contribution in shaping the diurnal rainfall over Bandung (Oigawa et al., 2017).

In the present study, we investigated one of the severe surface winds with the most devastating impact in Indonesia that destroyed ~ 305 residential and public building constructions and injured 5 people (CNN Indonesia, 2021). It occurred on 28 March 2021 on a small scale (~ 2 km) in Cimenyan, Bandung City, Indonesia (Detiknews, 2021; BNPB News, 2021). Due to the destructive impact of twigs broken from trees recorded at 15:40–16:00 LT by the amateur video (Ginanjar, 2021), the high wind reported by the BMKG reached 56 km h^{-1} (Tempo, 2021), categorized as Beaufort 8.

Given that the high wind was not part of the low-pressure system on a large scale over the area study, this single event is an ideal real case to investigate the responsible processes of generating the severely damaging wind in a limited area using a numerical model. Thus, we invoked the possible mechanism of the high wind, attributed to local and large-scale combinations as drivers of extreme wind without Tropical Disturbance (Choi & Tanurdjaja, 2002).

In this case, we assumed that the physical processes of the high wind event in the lesser latitudes refer to the solved theory of tornado-genesis in mid-latitudes. Since the tornado-related damaging wind over small areas has a relationship with quasi-linear convective systems (QLCS) and low-level meso-γ-scale vortices (Schenkman & Xue, 2016), the genesis of the small tornado might also be associated with both QLCS and mesovortex. Nevertheless, the QLCS could also be manifested as a bow-echo determined by the strengthening of mesovortices produced by the cold pool at the surface level (Atkins & Laurent, 2009a, 2009b).

The hypothesis of tornado genesis was applied in the present study using a numerical simulation with high-resolution Weather Research and Forecasting (WRF). We compared the simulation results between 1 km, 0.5 km, and 0.2 km grid spaces. Since we are also concerned about the sparse in-situ data in Indonesia, we deployed X-band non-doppler radar around the Bandung region. We used the results to validate the rainfall simulation to confirm the fine resolution in capturing the high wind event. As the first documentation of “puting beliung” based on a real case event, this present study could be a new insight into predicting the high wind over the Indonesia Maritime Continent.

2. Materials and Methods

Herein, we investigated the physical and dynamic processes of a high wind event over a limited area in Cimenyan, Bandung, Indonesia, by conducting a numerical study using a high-resolution WRF model into 0.2 km and 5 minutes for spatial and temporal resolutions, respectively. We designed two scenarios of numerical experiments to simulate the real event based on its resolution, microphysics scheme, and topography.

For the control numerical experiment, we used WRF-ARW model version 4.1.2 (Skamarock et al., 2008) with one-way nested domains consisting of a parent domain (D01) and three nesting domains (D02, D03, and D04), with a grid spacing of 3, 1, and 0.5 km, respectively. The parent domain was determined on a large-scale center of the western Maritime Continent (Fig. S1) according to recent studies that provided a

detailed validation for the configuration (Wang et al., 2015; Chen et al., 2018; Ruppert & Chen, 2020; Ruppert & Zhang, 2019; Yulihastin et al., 2023). The configuration schemes of the model used in the present study based on default combinations in WRF are exhibited in Table S1. Thus, since we assume that the high wind was associated with a bow echo, we also compared 1 and 0.5 km, incorporating an appropriate resolution for storm-resolving performance.

Moreover, as our concern was to simulate a strong surface wind (< 10 m), for the second scenario, we also improved the vertical resolution from 60 to 137 levels from the surface to the low level provided the Geopotential and Geometric heights, the temperature and density of the level based on the 1976 version of the International Civil Aviation Organization (ICAO) Standard Atmosphere. Here, to enrich the timing of initial and maximum bow echo, we tested the microphysical schemes and found Purdue Lin as an appropriate scheme. We also modified the input of topography by applying a 90 m grid spacing to enhance the shape of the bow echo.

Table 1
Configuration of the Weather and Research Forecasting model for simulating severe damaging wind associated with bow-echo activity over Cimenyan, Bandung, Indonesia, at horizontal resolutions of 9 km (D01), 3 km (D02), 1 km (D03), and 0.2 km (D04).

Region	D01	D02	D03	D04
Horizontal grids	201 × 201	202 × 202	202 × 202	251 × 251
Grid spacing (km)	9	3	1	0.2
Cumulus scheme	Betts–Miller–Janjic	Betts–Miller–Janjic	No-scheme	No-scheme
Vertical grid	60 layers	60 layers	60 layers	60 layers
Radiation	RRTMG longwave scheme RRTMG shortwave scheme	RRTMG longwave scheme RRTMG shortwave scheme	RRTMG longwave scheme RRTMG shortwave scheme	RRTMG longwave scheme RRTMG shortwave scheme
Microphysics	Purdue-Lin	Purdue-Lin	Purdue-Lin	Purdue-Lin
Surface layer Land surface	Revised MM5 Monin-Obukhov Unified Noah land-surface model	Revised MM5 Monin-Obukhov Unified Noah land-surface model	Revised MM5 Monin-Obukhov Unified Noah land-surface model	Revised MM5 Monin-Obukhov Unified Noah land-surface model
PBL	Yonsei University	Yonsei University	Yonsei University	Yonsei University
Initial boundary condition	FNL	FNL	FNL	FNL

Furthermore, to confirm the background condition in mesoscale during the real case event, we also revealed the hourly temperature black body (TBB) with 0.05° spatial resolution and precipitation data from Himawari (Bessho et al., 2016) and the Global Satellite Mapping of Precipitation (GSMaP) with 0.1° spatial resolution (Kubota et al., 2007), respectively. Notably, the convective index was calculated by subtracting the TBB from the threshold value of 220^{o}K, denoted as the lowest temperature in a cloud base (Chang et al., 2005).

Hence, to validate the dynamic processes in capturing the bow echo shape of rainfall simulated by the model, we revealed a 2-minute time interval of maximum reflectivity data as rainfall interpretation from the X-band radar. The X-band radar was a low-cost alternative to weather radar with simple features such as non-coherent, pulsed, single polarization (horizontal), non-Doppler, fixed antenna elevation (fan beam), and 6-kW peak power.

It is exclusively devoted to rain measurements and can produce one rain map in two seconds with a maximum range of 44 km and a range resolution of 120 m (Sinatra et al., 2021). Even with the limitations in technology, it is still utilized as a cost-effective alternative for precipitation measurement (Orellana-Alvear et al., 2019; Allegretti, 2021; Lo Conti et al., 2015). For rainfall observation purposes, the signal echo was processed through a clutter removal method (Awaludin et al., 2021), attenuation correction, volume correction, and conversion to radar reflectivity factor (Nugroho et al., 2018).

Two non-doppler radars and one Doppler radar are installed in the middle of the Bandung basin to provide better validation data for improving local rainfall forecasting products. Since the X-band radar reflectivity data was derived to capture the bow-echo shape over a limited area of Cimenyan, we used the two Automatic Weather Stations of Djunjunan and Ganesa sites data (Fig. 2) to validate the high wind event and other parameters such as rainfall and pressure to analyze the caused related to both convection and convergence processes.

3. Result and Discussion

3.1 High-wind Observed and Background Condition

The high wind (56 km h^{-1}) reported (Tempo.co, 2021) over Cimenyan in the black box area was concurrent by bow echo rainfall shape as depicted by maximum reflectivity by X-band radar located around 20 km from the extreme event location (Fig. 2a). The increase of surface wind (5–7 m s^{-1}) was accompanied by enhanced gust wind (~ 20 km h^{-1}) initiated from 12:00 LT and reached a maximum in the afternoon (48 km h^{-1}) on 28 March 2021.

The acceleration of gust wind was mainly caused by the drop of surface pressure during the time. Herein, the maximum high wind coincided with the rapid onset of heavy rainfall (~ 10 mm) associated with the maximum convective activity at 15:45 LT on 28 March 2021 (Fig. 2b). To ensure that the convection

relates to the mesoscale convective system, we need to explore synoptic analysis as a background condition during the extreme event episodes demonstrated in Fig. 3.

The synoptic condition in Fig. 3a shows that during the 25 March–1 April 2021, several vortices existed over the Indian Ocean in the western part and the Banda-Maluku seas in the eastern part of the IMC as a precondition in developing the Seroja tropical cyclone mentioned in the previous study (Yulihastin et al., 2023). Those large-scale disturbances could trigger the development of mesoscale convective systems remotely over the western part of the Indonesia Maritime Continent, particularly in south Sumatra-west Java.

The diurnal evolution of convective activities pronounced the deep convective cloud extensively and concentrated mainly over Lampung, Sumatra, and Java Sea from the middle of the night to early morning on 28 March 2021 (Fig. 3b). In the detailed time interval, the mesoscale of the early morning oceanic convection system over the Java Sea propagated northward and disappeared at 07:00 LT on 28 March 2021 (Figures not shown).

Less convection covered the entire domain from morning to mid-day on 28 March 2021. However, the period of extreme event (12:00–17:00 LT) was suggested as a precondition of the mesoscale convective system due to an unstable environment of atmospheric conditions. The black-body temperature data also indicated that the mesoscale convective complex tends to develop over the entire mainland of West Java in the nighttime (Fig. 3c).

Since we are mainly concerned with understanding the deep convection cloud development contributed to high wind over Cimenyan, we inspected the detailed evolution in a ten-minute evolution of cloud activity (Fig. 4). Figures 4a–f exhibited two convective cells in the west and east parts close to Cimenyan. However, the western convective cell suggested more contributed to creating high wind than the east convection system. Furthermore, the western cell was also demonstrated to rapidly develop from a single small cell to a mesoscale convection system.

3.2 Development of a Short-lived Bow Echo

The heavy rainfall recorded by maximum reflectivity described the bow-echo shapes with similar eastward orientation patterns from 15:24 to 16:02 LT (Figure not shown). A-hook-shaped echo, the so-called apex, was related to strong damage wind, as described in the previous studies (Wakimoto et al., 2006a, 2006b). However, features in the bow echo motion displacement vector calculated by optical flow (Hambali et al., 2020) demonstrated that double meso-γ-vortices (north and south meso-γ-vortices) existed from 15:48 to 16:06 LT (Fig. 5). In this case, the impacted high-wind area was located near the north meso-γ-vortex, similar cases to several previous studies (Zhiyong et al., 2016; Weisman et al., 1998; Davis & Galarneau, 2008).

While the maximum intensity of high wind related to the north meso-γ-vortex was developed, the bowing shape was opposite orientation from eastward (15:40–16:00 LT) to westward (16:02–16:12 LT). This

shift of bow-echo orientation primary was influenced by the alternation of vorticity from anti-cyclonic to cyclonic of the north meso-γ-vortex depicted at 15:54 LT on 28 March 2021.

This vortex indicated the end of a line segment of convective cells associated with strong vorticity between 2 and 4 km AGL during several hours of lifetime, as stated in the previous study (Zhiyong et al., 2016). Here, the bow echo life cycle recorded by radar reached 40 minutes before the bowing shape was broken as a straight line. Numerous studies also disclosed the relationship between bow-shape convective systems and the straight-line damaging surface wind or the so-called downbursts at the surface (i.e., Schenkman & Xue, 2016; Fujita, 1978; Johns & Hirt, 1987; Przybylinski, 1995; Wakimoto et al., 2003).

3.3 Role of Meso-γ-Vortices in Generating High Wind

To explore the genesis and possible mechanism for developing a short-lived bow echo and its relationship with meso-γ-vortices, we conducted high-resolution numerical simulations in spatial (1 and 0.5 km) and temporal (5 minutes). We discussed the results in further figures. Since we compared 1 and 0.5 km spatial resolutions, maximum precipitation over Cimenyan initiated from 14:34 to 15:34 LT (Figure not shown), and we compared both resolutions in capturing the bowing shape during the one-hour life cycle of rainfall depicted in Figure S2.

Since 1 km grid spacing captured QLCS with meridional orientation from 14:40 to 14:50 LT without bow echo shape (Fig. S2a), 0.5 km spatial resolution could simulate the initiated bow-echo shape at 14:50 LT with the eastward orientation location of the apex bow echo (Fig. S2b). This initial timing implied that the bow echo was simulated 34 minutes earlier than observed (15:24 LT). The previous study also failed to capture the exact timing and positioning (Xu et al., 2015). However, the location of the bow echo in this present study was still comparable with the observed. Previous recent studies also demonstrated discrepancies among different configuration schemes of WRF, otherwise simulated the same real cases (Atkins & St. Laurent, 2009a; Wheatley & Trapp, 2008). Herein, both spatial resolutions could capture the westward bow echo hook shape initiated at 15:10 LT with a 44-minute discrepancy with radar reflectivity (15:54 LT).

Given that the anti-cyclonic and cyclonic vorticities were not presented at the surface level, we need to explore reflectivity and wind simulated over 2 km AGL, as the prior study mentioned that strong vorticity appeared at this level (Fig. S3). The north and south anti-cyclonic meso-γ-vortices occurred at 14:40 LT. The bow echo was part of the north meso-γ-vortex, developed by meso-convergence. Furthermore, the intense easterly flow associated with the convection line over the eastern part of Cimenyan (107.7–107.8^{o}E) strongly connects with the bow echo. The convection line created a cyclonic vortex to the north, and as a consequence, the bow echo direction switched from eastward to westward at 15:10 LT on 28 March 2021. Several studies remarked that meso-γ-vortices developed on both sides of the bow apex that occasionally depicted asymmetries (Weisman & Trapp, 2003; Atkins et al., 2004; Atkins et al., 2005).

It should be noted that the model simulated a longer bow echo lifetime (50 minutes) than radar observation data (30 minutes). This lifetime of bow echo was categorized as short-lived, making the event hard to recognize. In this case, we need to simulate the possible mechanism of a short-lived bow echo associated with meso-γ-vortices, as found in the observational data. This creates more challenges in bow echo forecasting in Indonesia.

Thus, to improve the initial and maximum time of bow echo, we performed the 0.2 km grid spacing with Purdue Lin for a microphysical scheme and a 90 m topography resolution (Fig. 6). Notably, the improvement of initial (15:10 LT), maximum (15:30 LT), and decay (15:50 LT) of bow echo lifetime depicted a good agreement between simulated and observed reflectivity. The changing of direction orientation from eastward to westward of the book shape of the bow echo occurred a ten-minutes early (15:50 LT) in the model result was still comparable with the radar observation (16:00 LT). Figure 6 also suggested that the north and south mesovortices play a main role in developing the eastward bow echo, which corresponds to the control experiment (Fig. S3). However, the improved resolution experiment indicated the other bow echo existed over the east part of Cimenyan. The east bow echo existence associated with a new meso-convergence influenced the orientation of bow echo, as exhibited in Fig. 6 (15:45 to 15:50 LT).

As described in a previous study, damaging surface wind can be produced by combining the mesovortex and strong translational flow (Atkins & Laurent, 2009a; Wakimoto et al., 2006b). We further simulate the existence of a meso-γ-vortex by analyzing the anomalous vertical vorticities and surface wind vectors (20 m AGL) in Figure S4. The double meso-γ-vortices could be identified by anomalous positive and negative vertical vorticities, representing a strong vertical rotational wind with different orientations over the north of Cimenyan. The north meso-γ-vortex produced the small tornado, as reported by online media that the strong surface wind proceeded over north of Cimenyan area.

Meanwhile, as reported in previous observational studies, the prominent causes of significant wind damage were usually associated with the mesovortices in the bow echo system (Wheatley & Trapp, 2008; Weisman & Trapp, 2003; Atkins et al., 2004; Atkins et al., 2005). In this case study, we need vertical-cross-section analyses to examine the evolution of the bow echo maintenance (Fig. 7).

Herein, the meso-γ-vortex presence was indicated by anomalous positive (east-side) and negative (west-side) vertical vorticities initiated at 14:10 LT over Cimenyan (0.5–5 km) generated by meso-convergence over the surface level (< 2 km) which was identified by predominant meridional wind (Fig. 7a). This meso-γ-vortex ascended significantly at 15:30 LT, accompanied by strong updraft (Fig. 7b).

In addition, other meso-γ-vortices were also captured in the over and east side of the mountain areas, which enhanced the vertical flow of convection. It is important to note that the previous result for the opposite of bow-echo orientation occurred at 15:10 LT. This might be supported by changing the orientation of meso-γ-vortices rotation in both Cimenyan and mountain areas from 14:49 LT to 15:15 LT. It should be noted that the dynamic processes in developing bow echo initiated from strong updraft from

14:50 LT associated with enhancing cyclonic and anti-cyclonic vorticity at low-level troposphere (1–4 km height) over Cimenyan (107.6^{o}E) (Fig. 8).

Since initiating the bow echo over Cimenyan was disclosed by the strong updraft at the low level (recall: Fig. 8), it played a main role in enhancing the vertical vorticity during 15:00–15:30 LT (Fig. 9a), thus producing the sustained wind (Fig. 9b). The model result could capture the high wind > 56 km h^{-1} at 0.5 km at 15:20 LT. This high wind was associated with continuous rainfall onset and reached the maximum intensity (15 mm) at 15:30 LT (Fig. 9c), which was considerable with observed rainfall (recall: Fig. 2b).

As we are involved with the development of a column of cyclonic vorticity produced by the rotational wind, the vertical wind shear among three levels, 0, 3, and 6 km, represented surface, low, and middle of the troposphere, respectively, was demonstrated (Figs. S4a–d). The continued decline of the surface temperature from 25 to 20^{o} persisted from 13:30 LT to 16:30 (Fig S4a).

This decrease in temperature was associated with the strong vertical wind shear initiated from the surface to the mid-troposphere and attained maximum at 15:30 LT (Fig. S4b). The increase of wind shear evoking the surface updraft triggered instability over the upper levels (Fig. S4c). This updraft was also proven by increased surface-based convective available potential energy exhibited significantly and in phase with the most unstable CAPE (Fig. S4d). Conversely, the less downdraft CAPE exhibited that the strong updraft was not accompanied by downdraft outflow; thus, the high wind might not relate to a downburst. In addition, we are also concerned with demonstrating the analytical solution of the bow echo mesovortex as an ideal conceptual model applied in this case study (Fig. S5) using the green function derived in the Appendix.

4. Concluding remarks

Herein, we investigated the plausible mechanism of the high wind of Beaufort 8 scale (56 km h^{-1}) that occurred on 28 March 2021 in a limited area of Cimenyan district, Bandung, West Java, Indonesia. We combined observational and numerical methods to explore the physical and dynamic processes related to that severely damaging wind. Our results pointed out that the life cycle and possible mechanism of a short-lived (40 minutes) bow echo meso-γ-vortices could be described as follows (Figs. 10a–b):

1. An isolated bow echo was developed by four convective cells and generated by meso-convergence existence over the Bandung basin and surrounding extensive areas. The isolated bow echo is consistent with a previous study that demonstrated a large (80 km) and a long-lived (8 hours) bow echo was associated with a strong meso-β-scale convective system (Davis et al., 2004).
2. The development of a bow echo was previously influenced by the sustained wind, rapid heavy rainfall onset, and increased convective activity as a precondition of the mesoscale convective complex in the evening. On 28 March 2021, the double vortices existed over the Banda-Maluku seas of eastern Indonesia that were noticed as a precondition of Seroja tropical cyclogenesis (Yulihastin

et al., 2023). This large scale of circulation might also contribute to remoting the local of the extreme event in the western region of Indonesia.

3. An isolated bow echo was associated with meso-γ-vortices, the so-called meso-γ-vortex A and meso-γ-vortex B, over Cimenyan and mountainous areas in the eastern Cimenyan. In this case study, the meso-γ-vortex A over Cimenyan was generated by surface-level vorticity and significantly increased by the strong updraft over the low-level convergence. In a previous study, Xu et al. (2015) mentioned that severe straight-line winds were also found near the surface associated with mature and dissipated stages.
4. Specifically, the meso-γ-vortex over line-end vortices developed in strong vertical wind shear and most unstable convective energy, which triggered a column of cyclonic vorticity from the surface to the middle troposphere consistent with previous studies (Davis et al., 2008). This study detected the strong vorticity associated with circulation at 2–4 km AGL, corresponding to the prior study that the line-end vortex is often a relatively shallow feature confined to ~ 3 km (Weisman, 1993).
5. The main role of the line-end meso-γ-vortex A was manifested in the bow echo life cycle by creating the 180^{o} of reversal apex orientation from westward to eastward. This changing bow echo apex orientation indicated the vortex contribution while connecting with the convective line, thus producing the severely damaging wind as a part of the wind gust system.
6. The short-lived (~ 40 minutes) small tornado was found as a rotational updraft located in the end-line meso-γ-vortex A near the north of the bow echo apex over Cimenyan was maintained by a low-level meso-convergence and was supported by anomalous of vertical vorticity over mountainous regions.

The present study remarked that the high-resolution WRF model prevailed over an isolated bow echo and could simulate the precise location of bow echo over Cimenyan. It should be noted that the bow echo and high wind simulated have a good agreement with data observed in timing and intensity for 0.2 km grid spacing resolution with Purdue Lin microphysics scheme, a 90 m topography, and 137 vertical levels. It suggested that the 0.2 km grid spacing could simulate the bow echo associated with the high wind event in Indonesia, indicating that 0.2 km is the appropriate spatial resolution for capturing the storm-resolving model. Since we were also aware of the issue concerning the sparse in situ data in Indonesia, the X-band non-Doppler radar was noticed as a powerful observational measurement for detecting small-scale rainfall related to local circulation. Notably, due to the accelerating warming of surface temperature over the mainland and an imbalance of incoming solar radiation in the surface ground, the highly damaging wind associated with small tornados is expected to be frequent and intensify over the Indonesia Maritime Continent.

Declarations

Acknowledgments. The authors greatly acknowledge Dr. Nurjanna Joko Trilaksono for the discussion to improve the numerical experiment and Bandung Institute of Technology for providing the in-situ data of the AWS Ganesa. The present study supports the development of the forecasting product of the

Numerical-based prediction of Atmosphere-ocean Knowledge Using Deep Learning Artificial intelligence (NAKULA) at the Research Center for Climate and Atmosphere, National Research and Innovation Agency (BRIN). High-Performance Computing completed the simulations described in this study from the Computational Laboratory of Atmospheric Numerical Prediction (KRESNA) at the Research Center for Climate and Atmosphere, BRIN.

Author's contribution. Erma Yulihastin is the main contributor to this manuscript, who designed the conceptual research experiment, drafted the initial manuscript, revised it, and improved discussions and the overall content. Ibnu Fathrio was the main contributor who simulated the model and contributed to the significant findings. Ginaldi Ari Nugroho, Albertus Sulaiman, and Halimurrahman, were the main contributors to processing radar data in producing significant figures and schematic mechanisms as well as analytical solutions. Others contributed to producing corresponding figures to validate the model and supporting figures. All the authors were involved in discussions during the initial draft and review process and also read and approved the final manuscript.

Conflict of interest. The authors do not have any competing interests.

Funding. This study was supported by the National Research and Innovation Agency (BRIN) under the Program House of Research Organization of Electronica and Informatics with grant number 1/III.6/HK/2023.

References

1. Abdillah, M. R., Sarli, P. W., Firmansyah, et al.: Extreme Wind Variability and Wind Map Development in Western Java, Indonesia. Int. J. Disaster Risk Sci., 13, 465–480. (2022) https://doi.org/10.1007/s13753-022-00420-7.
2. Allegretti, M.: X-Band Mini Radar for Observing and Monitoring Rainfall Events. Atmos. Clim. Sci. 2, 290–297, (2021). DOI:10.4236/acs.2012.23026.
3. Atkins, N.T., Arnott, J.M., Przybylinski, R.W., Wolf, R.A., Ketcham, B.D.: Vortex Structure and Evolution within Bow Echoes. Part I: Single-Doppler and Damage Analysis of the 29 June 1998 derecho. Mon. Weather Rev. 132, 2224–2242, (2004).
4. Atkins, N.T., Bouchard, C. S., et al.: Damaging Surface Wind Mechanisms within the 10 June 2003 Saint Louis Bow Echo during BAMEX. Mon. Weather Rev. 133, 2275–2296, (2005).
5. Atkins, N.T., and Laurent, M. St.: Bow Echo Mesovortices. Part I: Processes That Influence Their Damaging Potential, Mon. Weather Rev. 137(5), pp 1497–1513. (2009). https://doi.org/10.1175/2008MWR2649.1.
6. Atkins, N. T., and Laurent, M. St.: Bow Echo Mesovortices. Part II: Their Genesis, Mon. Weather Rev. 137(5), pp 1514–1532. (2009). https://doi.org/10.1175/2008MWR2650.1.
7. Awaludin, A., Sinatra, T., Nugroho, G. A., and Nauval, F.: Clutter Removal Improvement of Marine Radar for Weather Observation, AIP Conference Proceedings, Bogor. 2366, 060023, (2021).

https://doi.org/10.1063/5.0060062.

8. Bessho, K., Date, K. Hayashi, M., et al.: An Introduction To Himawari-8/9— Japan's New-Generation Geostationary Meteorological Satellites, Journal of the Meteorological Society of Japan, 94, 151–183, (2016).
9. BNPB.: Geoportal Data Bencana Indonesia. https://gis.bnpb.go.id/. (2022). Last access: 9 February 2023.
10. BNPB New.: Angin Puting Beliung Terjang Pemukiman Warga Cimenyan, Kabupaten Bandung. https://www.bnpb.go.id/berita/angin-puting-beliung-terjang-pemukiman-warga-cimenyan-kabupaten-bandung-. (2021). Last access: 10 February 2023.
11. BPBD West Java.: Infografis Bencana. https://barata.jabarprov.go.id. Last access: 10 February 2023. (2022)
12. Cahyanti, R., Hutama, R. B., Ramdlon, R. H. W. et al.: Whirlwind Prediction Using Cloud Movement Patterns on Satellite Image. 2017 International Electronics Symposium on Knowledge Creation and Intelligent Computing (IES-KCIC), Surabaya, Indonesia, pp. 252–257. (2017) doi: 10.1109/KCIC.2017.8228595.
13. Chang, C., Harr, P.A., and Chen, H.: Synoptic Disturbances over the Equatorial South China Sea and Western Maritime Continent during Boreal Winter. Mon. Wea. Rev., 133, 489–503, (2005). https://doi.org/10.1175/MWR-2868.1.
14. Chen, X., Pauluis, O. M., and Zhang, F.: Atmospheric overturning across multiple scales of an MJO event during the CINDY/DYNAMO campaign. Journal of the Atmospheric Sciences, 75, 381–399. (2018) https://doi.org/10.1175/JAS-D-17-0060.1.
15. Choi, E. C. C., and Tanurdjaja, A.: Extreme Wind Studies in Singapore. An Area With Mixed Weather System, Journal of Wind Engineering and Industrial Aerodynamics, 90(12), 1611–1630. (2002). DOI:10.1016/S0167-6105(02)00274-X.
16. CNN Indonesia.: Puting Beliung Cimenyan Bandung: 298 Rumah Rusak, 5 Luka https://www.cnnindonesia.com/nasional/20210329202916-20-623590/puting-beliung-cimenyan-bandung-298-rumah-rusak-5-luka. (2021). Last access: 14 February 2023.
17. Davis, C. A., and Galarneau Jr, T. J.: The Vertical Structure of Mesoscale Convective Vortices, J. of the Atm. Sci, 66, (2008). doi: 10.1175/2008JAS2819.1.
18. Davis, C., N. Atkins, et al.: The Bow Echo and MCV Experiment: Observations and Opportunities. Bull. Am. Meteorol. Soc. 85, 1075–1093, (2004).
19. Detiknews.: Angin Puting Beliung Terjang Sejumlah Rumah di Cimenyan Bandung. https://news.detik.com/berita-jawa-barat/d-5511411/angin-puting-beliung-terjang-sejumlah-rumah-di-cimenyan-bandung. (2021). Last access: 10 February 2023.
20. Fujita, T. T.: Manual of Downburst Identification for Project Nimrod. Satellite and Mesometeorology. Res. Pap. 156. Dept. of Geophysical Science, University of Chicago (104 pp [NTISPB-286048]) (1978).

21. Ginanjar, R.: Angin Puting Beliung di Cimenyan Bandung. (28 March 2021). https://www.youtube.com/watch?v=00VZvmoglcQ. Last access: 10 February 2023.
22. Hambali, R., Legono, D., and Jayadi, R.: The Application of Pyramid Lucas-Kanade Optical Flow Method for Tracking Rain Motion Using High-Resolution Radar Images. Jurnal Teknologi. 83(1), 105–115, (2020).
23. Johns, R. H., and Hirt, W. D.: Derechos: Widespread Convectively Induced Windstorms. Weather and Forecasting. 2(1), pp. 32–49, (1987).
24. Kubota, T., Shige, S., Hashizume, H., et al.: Global Precipitation Map Using Satellite-Borne Microwave Radiometers by the GSMaP Project: Production and Validation, IEEE Transactions on Geoscience and Remote Sensing, 45, 2259–2275, (2007).
25. Lo Conti, F., Francipane, A., Pumo, D., and Noto, L. V.: Exploring Single Polarization X-Band Weather Radar Potentials for Local Meteorological and Hydrological Applications. Journal of Hydrology. 531, 508–522. (2015). https://doi.org/10.1016/j.jhydrol.2015.10.071.
26. Lumbangaol, A., and Munandar, A.: Atmosphere Dynamic Analysis of Hail and Whirl Wind in Cianjur Regency, West Java (Case Study November 07, 2016). The Proceedings of 1st International Conference on Science, Matemathics, Enviroment, and Education (ICoSMEE), Surakarta. (2018)
27. Nugroho, G.A., Sinatra, T., Trismidianto, and Fathrio, I.: Application of Rain Scanner SANTANU and Transportable Weather Radar In Analyze of Mesoscale Convective System (MCS) Events over Bandung, West Java, IOP Conf. Ser.: Earth Environ. Sci. 149 012058, (2018). DOI 10.1088/1755 – 1315/149/1/012058.
28. Oigawa, M., Matsuda, T., Tsuda, T., and Noersomadi, N.: Coordinated Observation and Numerical Study on a Diurnal Cycle of Tropical Convection over a Complex Topography in West Java, Indonesia. Journal of the Meteorological Society of Japan, 95(4), p. 261–281. (2017) https://doi.org/10.2151/jmsj.2017-015.
29. Orellana-Alvear, J., Célleri, R., Rollenbeck, R., and Bendix, J.: Optimization of X-Band Radar Rainfall Retrieval in the Southern Andes of Ecuador Using a Random Forest Model. Remote Sensing. 11, 1632, (2019). https://doi.org/10.3390/rs11141632.
30. Prakosa, M.G., and Nurjani, E.: Analysis of Convective Cloud Presence Surrounding Whirlwind Events in Yogyakarta, Indonesia. Proceedings Volume 12082, Seventh Geoinformation Science Symposium 2021. (2021) https://doi.org/10.1117/12.2617507
31. Przybylinski, R.W.: The Bow Echo. Observations, Numerical Simulations, and Severe Weather Detection Methods. Weather Forecast. 10, 203–218, 9, (1995).
32. Ruppert, J. H., Jr., and Chen, X.: Island Rainfall Enhancement in the Maritime Continent. Geophysical Research Letters, 47. (2020) https://doi.org/10.1029/2019GL086545.
33. Ruppert, J. H., Jr., and Zhang, F.: Diurnal Forcing and Phase Locking Of Gravity Waves in the Maritime Continent. Journal of the Atmospheric Sciences, 76, 2815–2835. (2019) https://doi.org/10.1175/JAS-D-19-0061.1.

34. Schenkman, A.D., and Xue, M.: Bow-echo Mesovortices: A Review, Atmospheric Research, 170, pp 1–13. (2016). https://doi.org/10.1016/j.atmosres.2015.11.003.
35. Sinatra, T., Awaludin, A., Nauval, F., and Purnomo, C.: Calibration of Spatial Rain Scanner using Rainfall Depth of Rain Gauges, IOP Conference Series: Earth and Environmental Science, Jakarta, 893 012064, (2021). DOI 10.1088/1755 – 1315/893/1/012064.
36. Skamarock, W. C., Klemp, J. B., et al.: A Description of the Advanced Research WRF Version 3 (No. NCAR/TN-475 + STR). University Corporation for Atmospheric Research. (2008) doi: 10.5065/D68S4MVH.
37. Tempo.: Kronologis Puting Beliung Cimenyan Bandung Dilihat dari Data Satelit, https://tekno.tempo.co/read/1447387/kronologis-puting-beliung-cimenyan-bandung-dilihat-dari-data-satelit. (2021). Last access: 14 February 2023.
38. Wakimoto, R. M., Hanne, V. M., David, C. D., and Howard, B. B.: The Kellerville Tornado during VORTEX: Damage Survey and Doppler Radar Analyses, Monthly Weather Review, 131(10), 2197–2221, (2003). DOI: https://doi.org/10.1175/1520-0493(2003)131<2197:TKTDVD>2.0.CO;2.
39. Wakimoto, R. M., Murphey, H. V., Davis, C. A., and Atkins, N. T.: High winds generated by bow echoes. Part II: The Relationship between the Mesovortices and Damaging Straight-Line Winds. Mon. Weather Rev. 134, 2813–2829, (2006).
40. Wakimoto, R. M., Murphey, H. V., Nester, A., Jorgensen, D. P., and Atkins, N. T.: High Winds Generated By Bow Echoes. Part I: Overview of the Omaha Bow Echo 5 July 2003 Storm during BAMEX. Mon. Weather Rev. 134, 2793–2812, (2006).
41. Wang, S., Sobel, A. H., et al.: Regional Simulation of the October and November MJO Events Observed During the CINDY/DYNAMO Field Campaign At Gray Zone Resolution. Journal of Climate, 28, 2097–2119. (2015) https://doi.org/10.1175/JCLI-D-14-00294.1.
42. Weisman, M. L.: The Genesis of Severe, Long-lived Bow Echoes. J. Atmos. Sci., 50, 645–670, (1993).
43. Weisman, M. L., and Davis, C. A.: Mechanisms for the Generation of Mesoscale Vortices within Quasi-Linear Convective Systems, J. Atm. Sci., 55, 2603–2622, (1998).
44. Weisman, M.L., and Trapp, R. J.: Low-Level Mesovortices within Squall Lines and Bow Echoes. Part I: Overview and Dependence on Environmental Shear. Mon. Weather Rev. 131, 2779–2803, (2003).
45. Wheatley, D. M., and Trapp, R. J.: The Effect of Mesoscale Heterogeneity on the Genesis and Structure of Mesovortices within Quasi-Linear Convective Systems. Mon. Weather Rev. 136, 4220–4241, (2008).
46. Xu, X., Xue, M., and Wang, Y.: Mesovortices within the 8 May 2009 Bow Echo over Central US: Analyses of the Characteristics and Evolution Based on Doppler radar Observations and a High-Resolution Model Simulation. Mon. Weather Rev. 143, 2266–2290, (2015).
47. Yulihastin, E., Taofiqurohman, A., Fathrio, I. et al. Evolution of double vortices induce tropical cyclogenesis of Seroja over Flores, Indonesia. Nat Hazards 117, 2675–2692 (2023). https://doi.org/10.1007/s11069-023-05961-8.

48. Zhiyong, M., Yao, D., Bai, L., Zheng, Y., et al.: Wind Estimation Around the Shipwreck of Oriental Star Based on Field Damage Surveys and Radar Observations. Sci. Bull., 61(4), 330–337, (2016). https://doi.org/10.1007/s11434-016-1005-2.

Figures

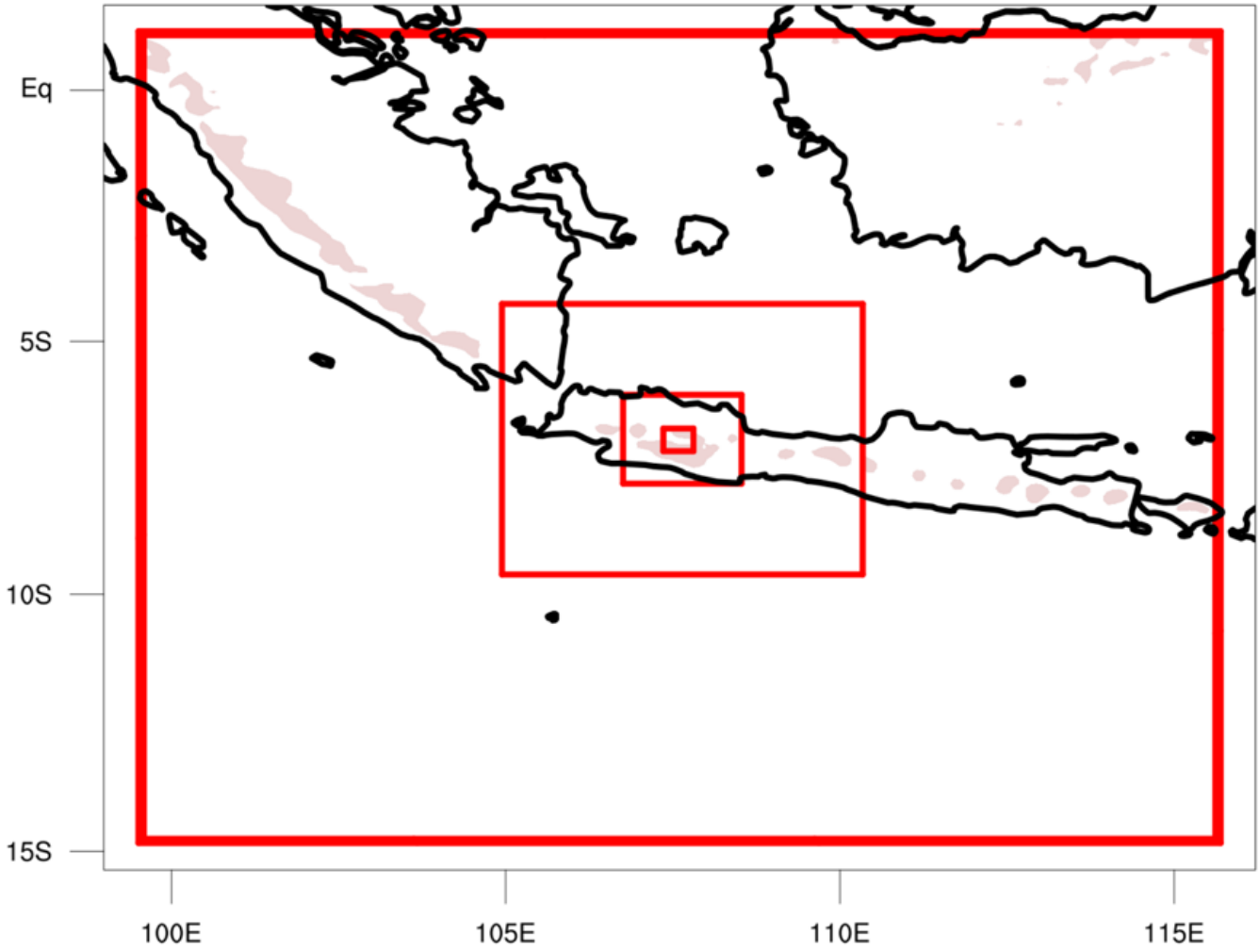

Figure 1

Configuration of model domains for simulating a bow echo meso-γ-vortex over Cimenyan, Bandung City, West Java province, Indonesia. The red boxes indicate the first (D01), second (D02), third (D03), and fourth (D04) domains, having horizontal resolutions of 9, 3, 1, and 0.2 km, respectively. The third and fourth domains represented West Java and Bandung regions. The pink color shaded indicated a rugged topography in the whole domain.

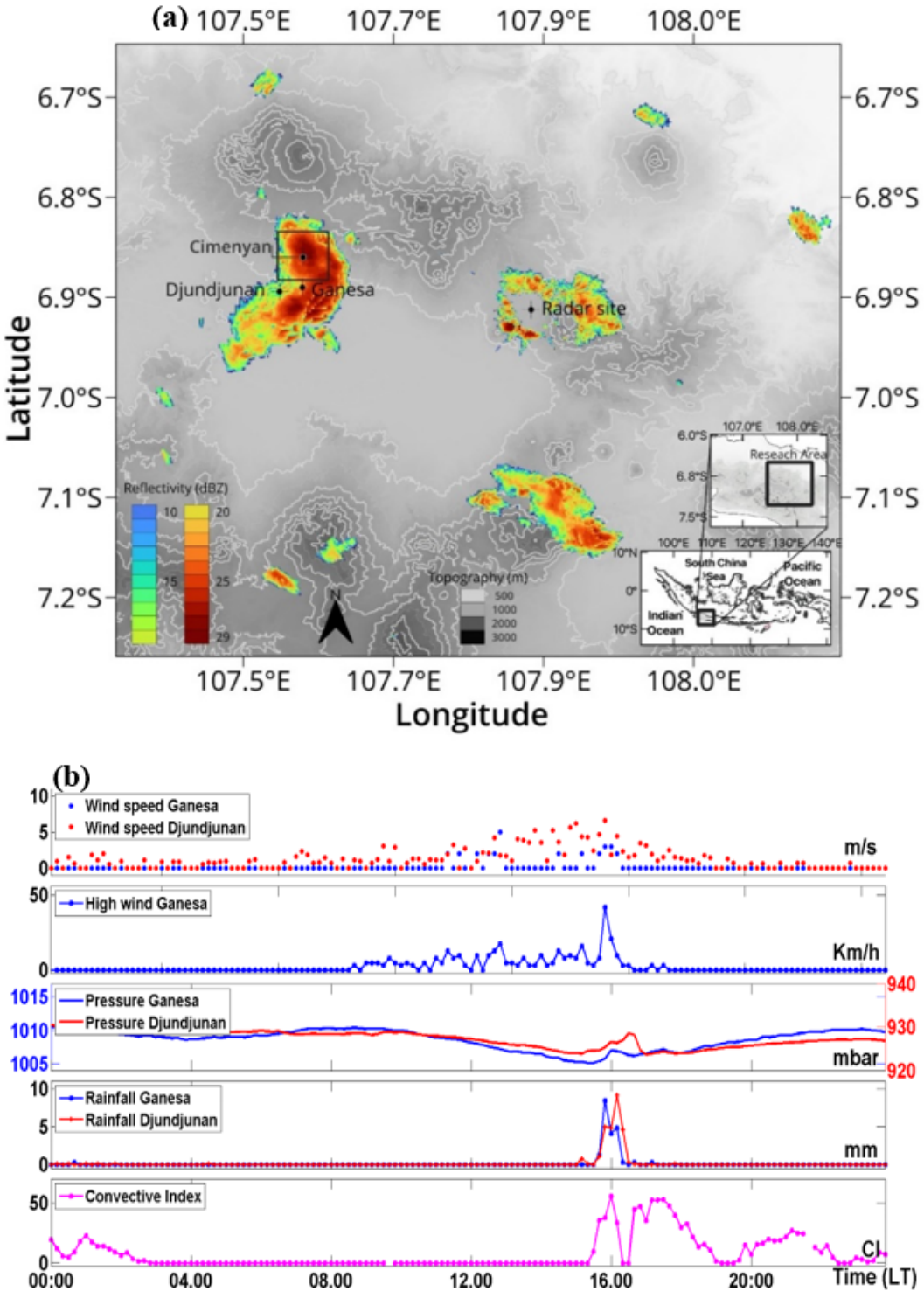

Figure 2

(a) A map showing Cimenyan and the surrounding area of interest and Indonesia was depicted as the inset, with coastlines, topographic contours, and maximum bow echo (shaded) during high wind event (15:48–15:58 LT). The black dots of Djunjunan and Ganesa indicated locations of Automatic Weather Stations, and the solid black box represented area-averaged of severely damaging wind impact (6.83°–6.89°S; 107.63°–107.68°E). The convective index derived from the Himawari satellite was calculated

around the area impacted (6.9°S;107.52°E) exhibited in Fig. 1b. (b) Time series of rainfall, surface pressure, wind speed, high wind derived from AWS stations of Djunjunan and Ganesa. The convective index was calculated using 220 K as a TBB threshold from Himawari satellite data following (Chang et al., 2005).

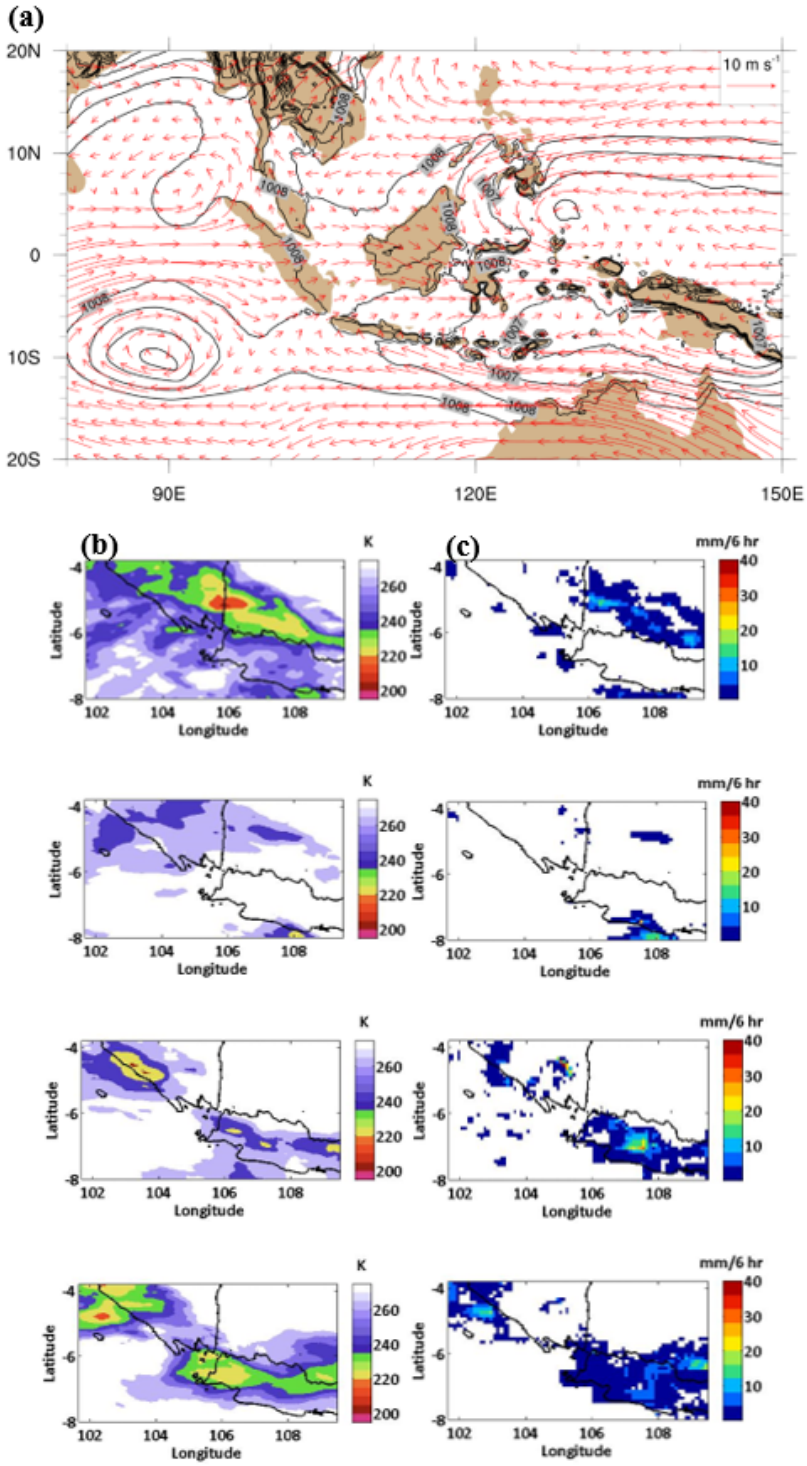

Figure 3

(a) A spatial daily average of mean sea level pressure (contour) and wind (vector) at 925 mb during 25 March–1 April 2021 from ERA5 reanalysis data. (b) Upper-to-lower panels: a spatial diurnal average on 28 March 2021 during 00:00–05:00, 06:00–11:00, 12:00–17:00, 18:00–23:00 LT for an hourly averaged black-body temperature (TBB) derived from Himawari satellite imageries. (c) It is the same as (b) but for a 6-hour rainfall accumulation retrieved from the GSMaP satellite.

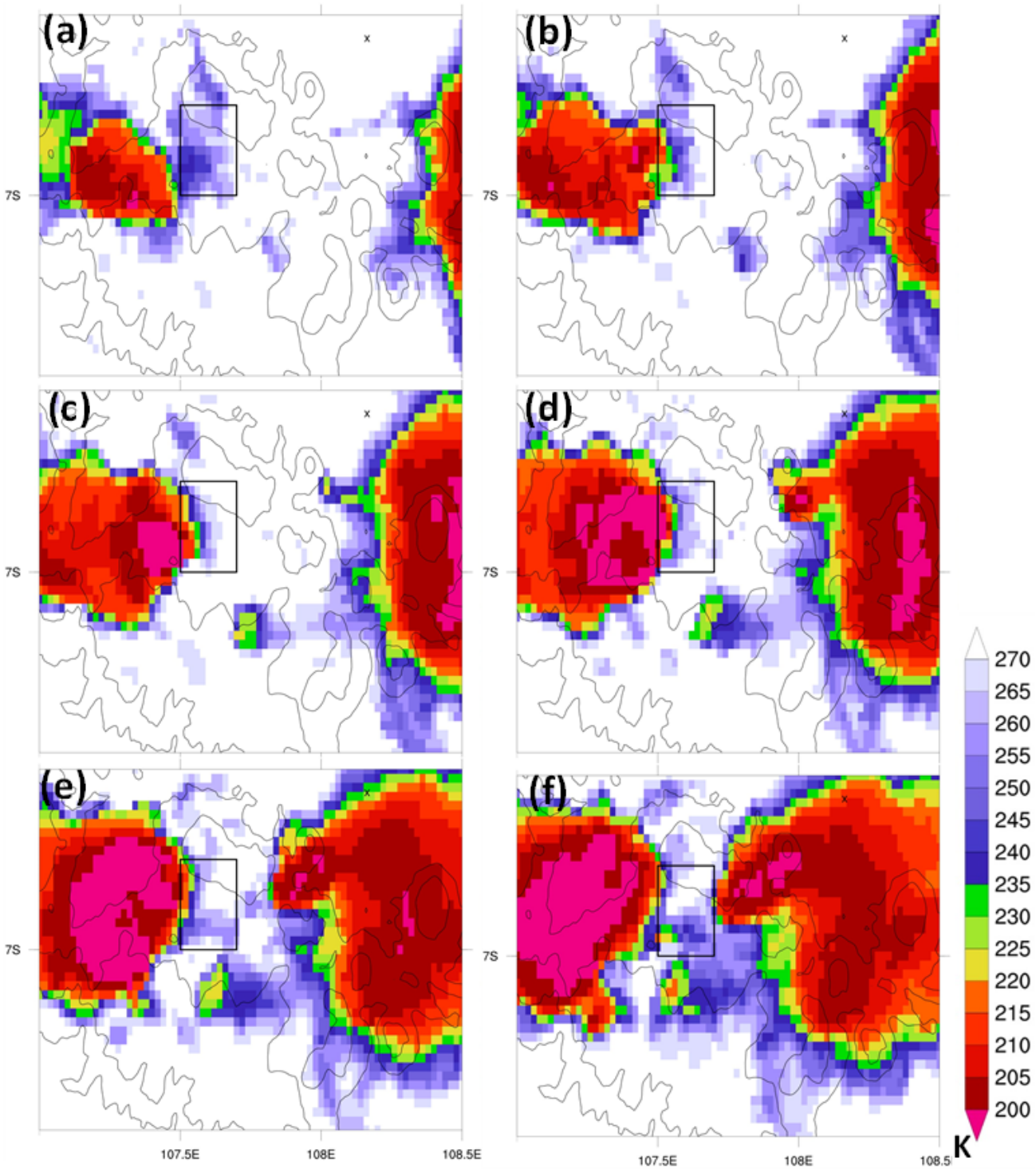

Figure 4

(a–f) A ten-minute evolution of averaged black-body temperature (TBB) derived from Himawari satellite imageries on 28 March 2021 (15:30 to 16:20 LT). The solid black box indicated the area impacted by high wind (Cimenyan, Bandung, West Java).

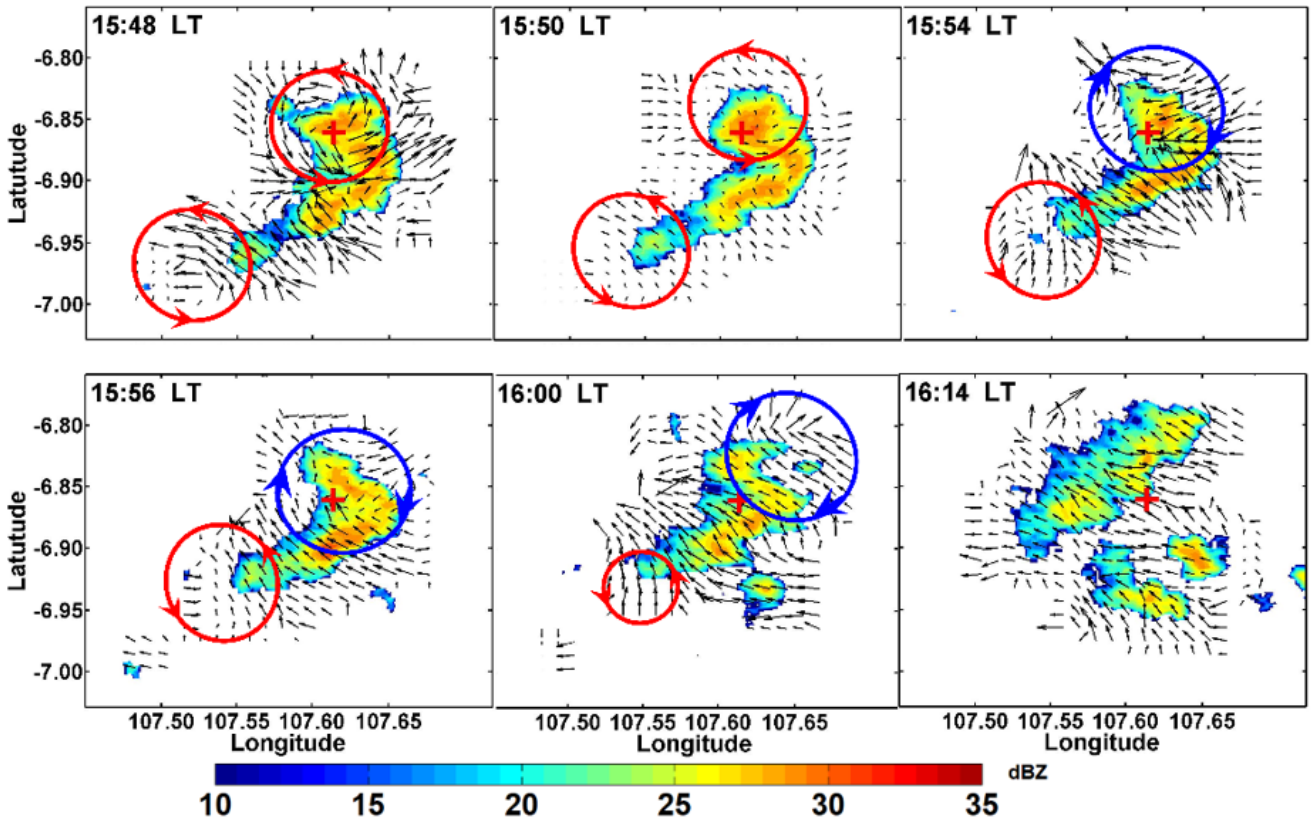

Figure 5

Same as Fig.4 (c) but for X-Band non-Doppler radar overlaid with bow echo motion vector during 15:48–16:20 LT on 28 March 2021. The black arrow represents the motion vector. The motion vector is derived from two successive radar reflectivity images, each having a two-minute temporal resolution. Blue and red circles represent the double vortices, with the arrow direction representing the clockwise and anticlockwise direction. The red plus sign indicates the severe wind location.

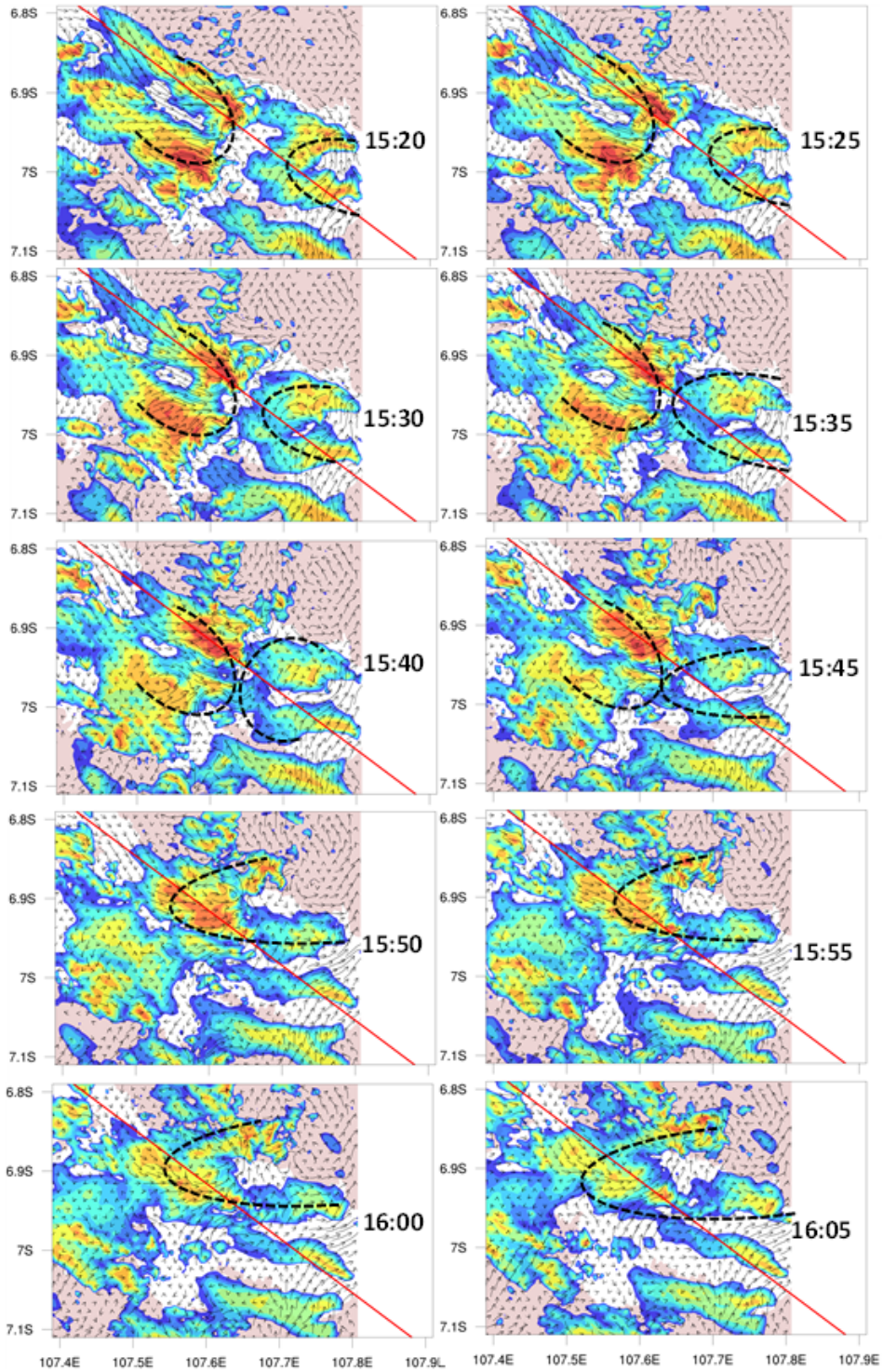

Figure 6

Same as Fig. S2, the improved resolution of 0.2 km grid spacing and Purdue Lin of the microphysical scheme (recall: Table 1).

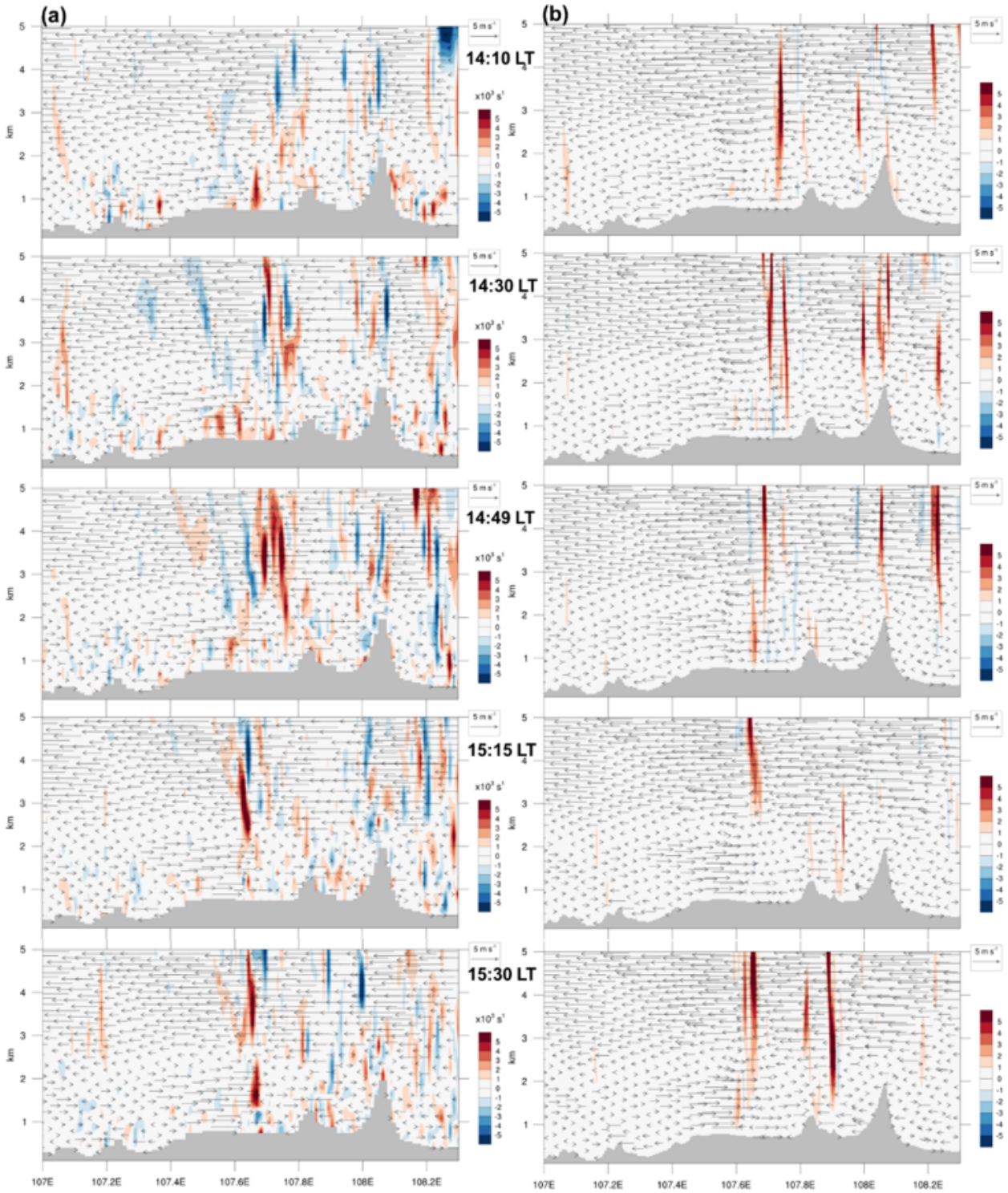

Figure 7

Height–Longitude cross-sections over transect line (refer to lines in Fig. 6) during 14:10 –15:30 LT for (a) zonal wind vector and maximum vertical vorticity (s^{-1}, shaded), (b) same as (a) but for vertical velocity (m s^{-1}). The high wind location over Cimenyan (107.6^{o}E).

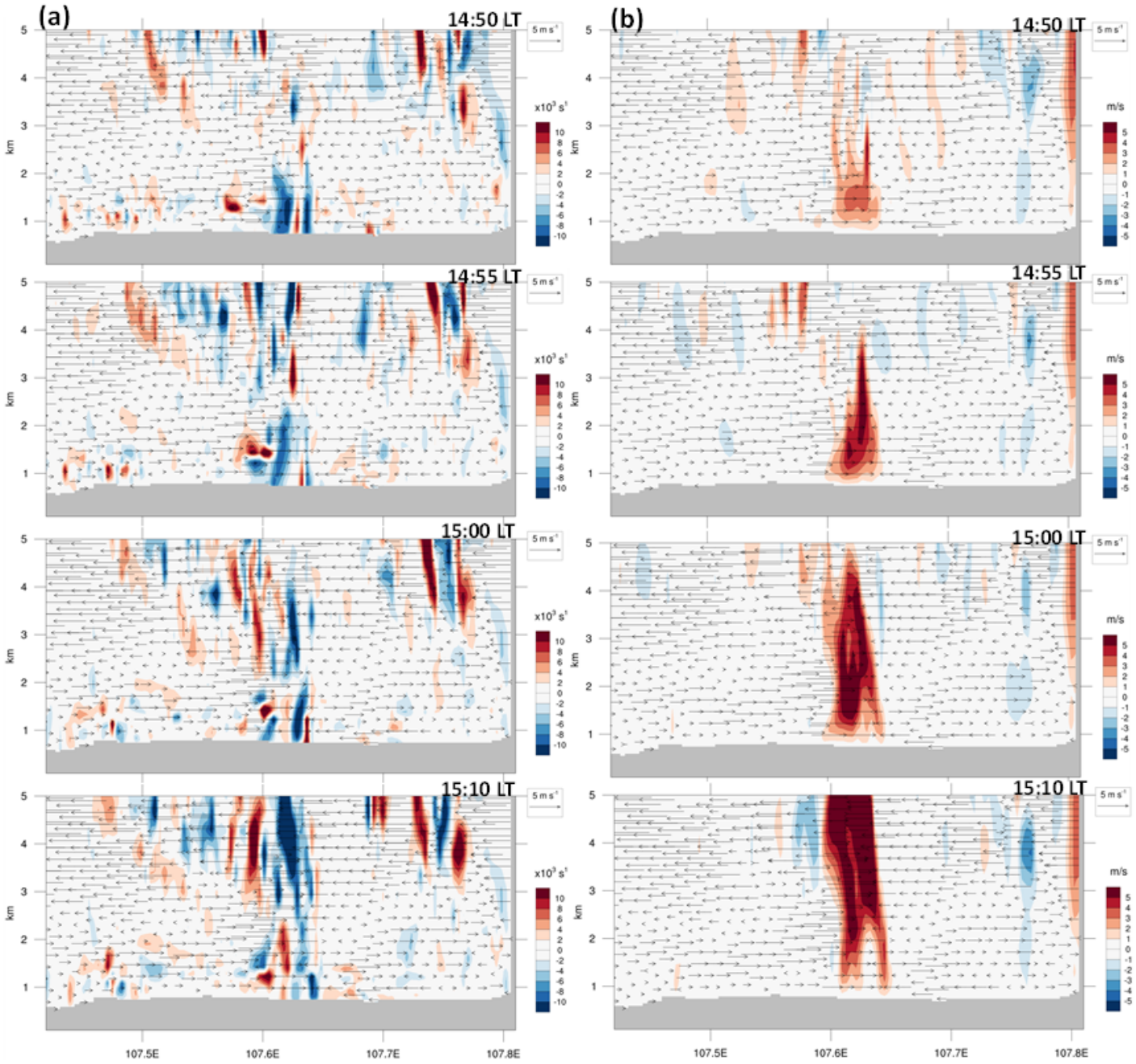

Figure 8

Same as Fig. 7, but for an improved high-resolution scenario from 14:50 to 15:10 LT.

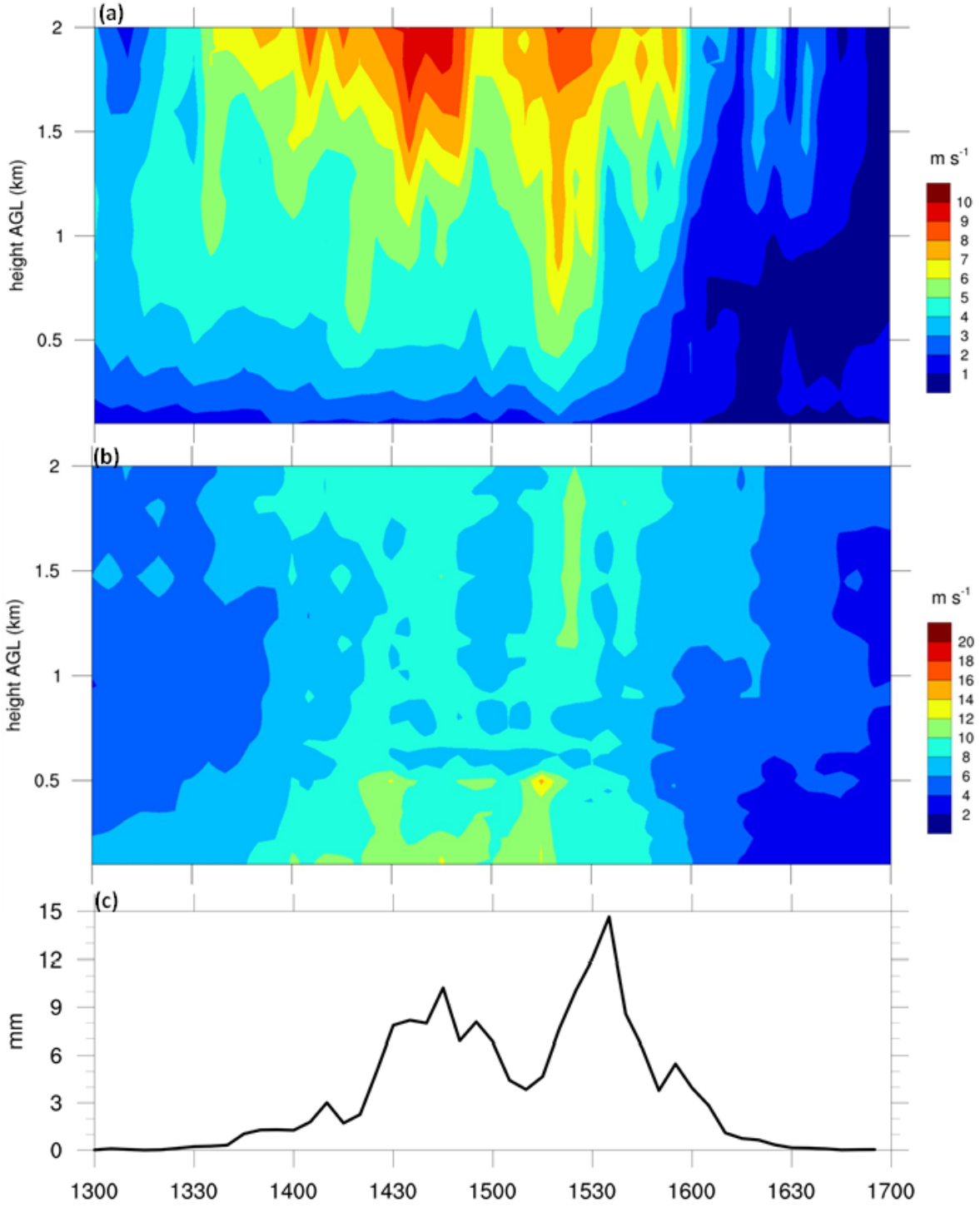

Figure 9

Time–height profiles around Cimenyan (6.9°S, 107.6°E) from 13:00 to 17:00 LT for (a) maximum vertical velocity (m s^{-1}), (b) zonal wind, and (c) precipitation.

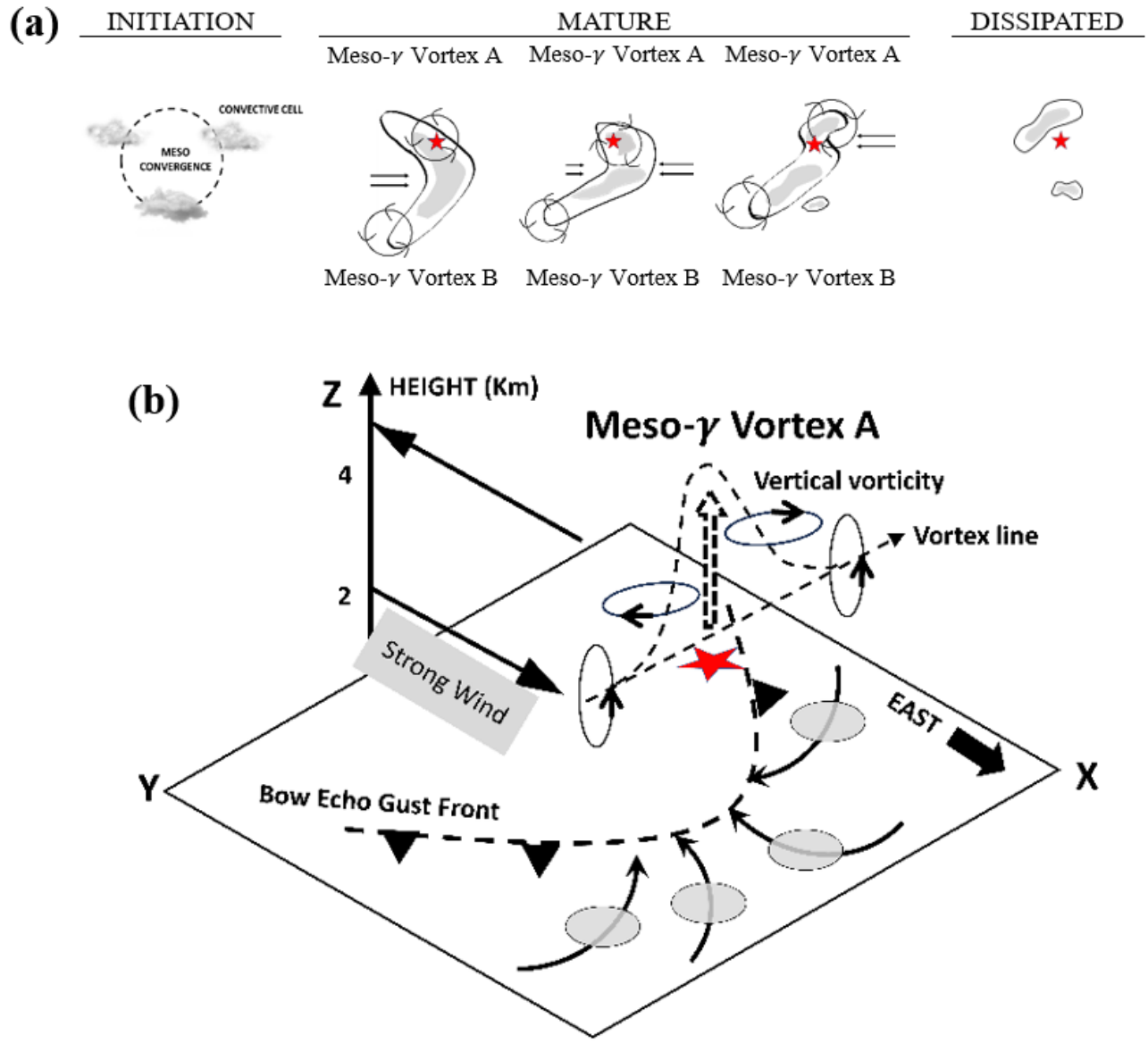

Figure 10

The schematic diagram for (a) the life cycle of bow echo meso-γ-vortices, (b) a 3-dimensional mechanism of a high wind associated with the development of bow echo meso-γ-vortices. The red star indicated the area of interest over Cimenyan.

Supplementary Files

This is a list of supplementary files associated with this preprint. Click to download.

- APJASEYHsupplement091023.docx
- Appendix.docx